Volume 18
Number 3
22 January 2026
Pages 1107-1678

Nanoscale

rsc.li/nanoscale

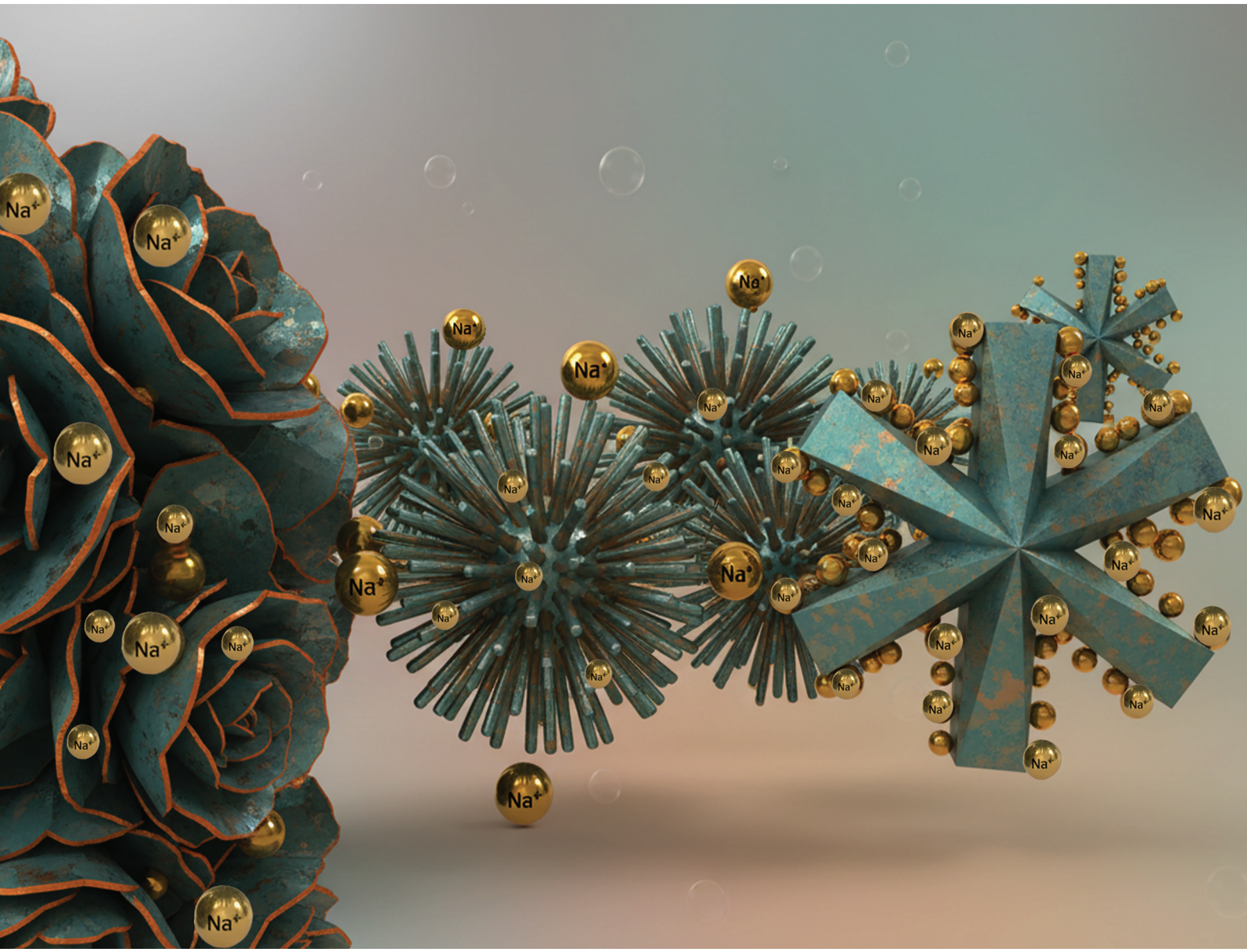

ISSN 2040-3372

ROYAL SOCIETY OF CHEMISTRY

PAPER
Luis R. De Jesús Báez *et al.*
On the crystal growth of vanadyl hydroxide (VOOH) with six-fold arms morphology

NCNST

Nanoscale

PAPER

View Article Online
View Journal | View Issue

Cite this: *Nanoscale*, 2026, **18**, 1335

On the crystal growth of vanadyl hydroxide (VOOH) with six-fold arms morphology

Jayanti Sharma, [a] Thomas J. Kolpack,[a] Karla M. Pérez Colón,[b] Mayuresh Janpandit,[a] Chloe Viyannalage, [a] Yuguang C. Li [a] and Luis R. De Jesús Báez *[a]

Received 30th June 2025,
Accepted 29th October 2025

DOI: 10.1039/d5nr02771c

rsc.li/nanoscale

Fundamental understanding of microstructure evolution during nucleation and growth of ternary materials is of utmost importance for the development of the next generation of functional devices. Case in point, growth of semiconducting particles with six-fold symmetry, star-shaped, could serve as an innovative morphology for application in neuromorphic, energy storage, and heterogenous catalysis devices. Herein, we present the discovery of how the synthetic route to produce orthorhombic star-shaped vanadyl hydroxide (VOOH) by using a hydrothermal reaction of orthovanadate and thioacetamide in an alkaline solution is highly dependent on time. For example, we observe that at 36 h, we produce VS_2 nanosheets with VOOH at the surface. A 60 h of reaction produce VOOH rods clustered in a single nucleating point and at 84 h of reaction VOOH stars can be observed in combination of clustered materials. Our current hypothesis stands that the clustered rods are a product of a condensation reaction between the vanadate precursor whereas the stars are seeded by the hexagonal symmetry of VS_2 and further oxygenation and reduction of the vanadium center. Furthermore, we also elucidate the fundamental electrochemical behavior of these nanoparticles as capacitive electrodes for sodium-ion devices.

[a]*Department of Chemistry, University at Buffalo, SUNY, Buffalo, NY 14260, USA. E-mail: ldjesus@buffalo.edu*
[b]*Department of Chemistry, University of Puerto Rico at Cayey, Cayey, 00736 Puerto Rico*

Luis R. De Jesús Báez

Born and raised in Puerto Rico, Luis obtained his B.S. in chemistry from UPR-Cayey. His Ph.D. was completed in TAMU under supervision of Prof. Banerjee with his thesis celebrated with several accolades including the IUPAC-Solvay International Award for Young Chemists. He then completed his postdoctoral work in Prof. Mallouk's lab in UPenn as a Provost Postdoctoral Fellow. Luis is currently an assistant professor in the Department of Chemistry of the University at Buffalo exploring materials in energy storing and catalytic devices. He has been awarded the 3 M NTFA, Young Observer to IUPAC, and Scialog: NES and Automated Laboratories Fellowships.

1. Introduction

Controlling nucleation and growth phenomena that access morphologies that deviate from traditional symmetries and fall into more complex structures can serve as an avenue to tailoring emergent properties.[1–3] Thus, understanding thermodynamic and kinetic mechanisms that direct morphology are key to meet this goal of tailoring properties *via* morphology control.[4–8] With that said, synthetic techniques that reliably alter morphology of a desired material while separating the thermodynamic and kinetic contributions to it are not trivially found and are needed to provide a template to understand nucleation and growth of anisotropic solid morphologies.

As a case in point, current synthetic efforts that seek to fundamentally understand morphology control of solids rely on the inclusion of a seed. In an unseeded nucleation and growth process, nucleation is purely dominated by thermodynamics models, *i.e.*, classical nucleation theory (CNT), where the Gibbs free energy of the system is minimized starting at a critical cluster size, r_c, which defines the nuclei.[9] This is immediately by a rapid self-nucleation of additional seeds that then start coalescing to grow in a resulting particle. Nevertheless, a seeded approach allows for the deconvolution of both the nucleation and growth components that contribute to different morphologies.[10–12] By altogether removing complex nucleation processes, the usage of a seed guides the growth

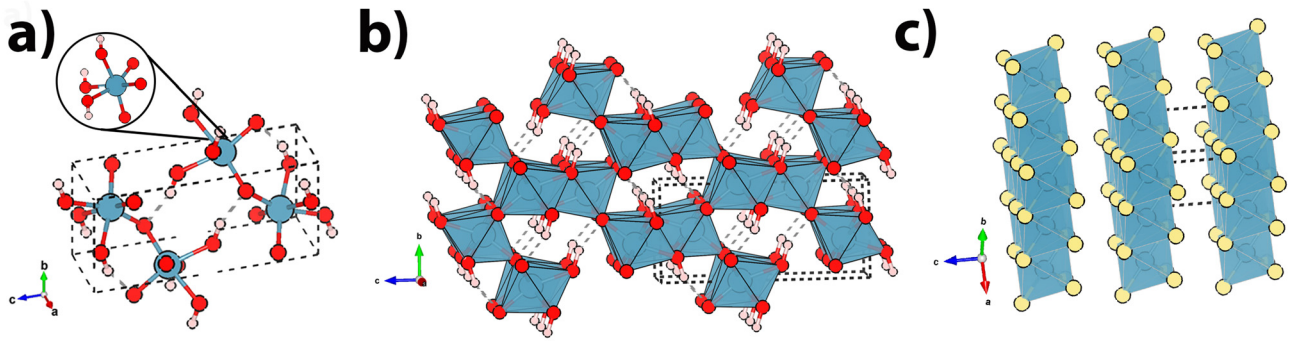

Fig. 1 (a) Unit cell for the crystal structure of montroseite VOOH where the pseudo-octahedral coordination environment is highlighted. (b) Supercell structures for VOOH projected along [101] and (c) VS_2 projected along the [111].

processes allowing for a better control, and understanding, of the resulting morphology.[13] Moreover, this approach has consistently demonstrated to work in the formation of unconventional morphologies.[5,6,12–14]

While this approach serves as an appropriate method to guide morphologies, the availability of ideal seeds limits the number of possible reactions and thus limit the scalability of this method. Moreover, nucleation and growth processes also play an important role in defect engineering.[15,16] For example, different types of crystal defects can tune the electrode performance in batteries[16,17] by providing ample actives sites for insertion processes. One such case is twin boundaries, where these defects are planar defect which exist at an interface of homogenous regions of materials and exhibit in the form of boundaries.[15,16] Considerable number of twin boundary defects has the potential of not only enhancing the ionic diffusion in electrode materials for batteries but also increase the number of active sites.[16] Herein we discuss the synthetic conditions and a proposed nucleation and growth processes that lead to a six-arms morphology of a transition-metal oxyhydroxide: vanadyl hydroxide (VOOH). This work demonstrates the need to explore synthetic routes that furnish alternative morphologies and sequentially introduce defects without the need of a seed to tune the electrochemical performance an electrode for advanced energy storage systems.[16,18,19]

To this end, the rich chemistry of vanadium offers a diverse range of valence states (from −1 to +5) which contribute to the myriad options of V-based materials with different compositions and structural frameworks.[14,20–26] Moreover, these V-based materials serve as an ideal system to explore the relationship between changes in oxidation state, morphology, and crystal structures with tunability of properties.[24,27,28] For example, low-dimensional layered structures of 3d transition-metal (oxy)hydroxides, *e.g.*, nickel oxyhydroxide and iron oxyhydroxide (FeOOH), are part of a family of materials with a structural library that spans different polymorphs (such as the orthorhombic and tetragonal crystal systems),[29–31] options of morphologies (nanosheet, nanorod, or nanosphere) while demonstrating excellent electrochemical performance, due to their high conductivity, stability, and abundant active sites.[31,32] In comparison, the montroseite structure was first discovered in 1949 as a new polymorph for VOOH by Stieff, Stern, and Girhard.[33] This polymorph of VOOH is comprised of a pseudo-octahedrally (Fig. 1a) V network of corner and edge-sharing O^{2-} and OH^- to form where stacking of double octahedral chains creates a rectangular-shaped tunnel structure along the *c*-axis (Fig. 1b). Curiously, a perusal of the literature highlights two common morphologies for VOOH: hollowed spheres or spherically clustered rods.[28,33–35]

Herein we report on the relationship between the extent of reaction time with the morphology of vanadyl hydroxide (VOOH) crystallites. We also report on the nucleation and growth mechanism behind the morphology changes of the crystallite across time and evaluate the electrochemical behaviour in relation to the morphology. We found that for the classical reaction between of sodium orthovanadate and thioacetamide initially form layered VS_2 (Fig. 1c), there is a time dependence to the product where VS_2@VOOH sheets transform to VOOH clusters who then lead to the nucleation and growth of vanadium nanostars. To the best of our knowledge, there are no reports on VOOH stars morphology. We hypothesize that free hydroxylated complexes with rods morphology that strip from the clusters undergo an olation followed by an oxolation process, which correspond to the formation of a hydroxyl bridge between two metals (M–OH–M bridging) and oxo bond between two metals (M–O–M bond), respectively, ultimately driving the assembly into star-like architectures (shown in Fig. S1).[36,37]

2. Experimental section

2.1. Materials and synthesis of VS_2 and VOOH structures

All the reagents used in this work are of analytical grade and were used as received without further purification. Sodium orthovanadate, Na_3VO_4 (purity 99%, CAS: 13721-39-6), sodium metavanadate, $NaVO_3$ (purity 96%, CAS: 13718-26-8), thioacetamide, C_2H_5NS (purity >98%, CAS: 62-55-5), sodium hydrox-

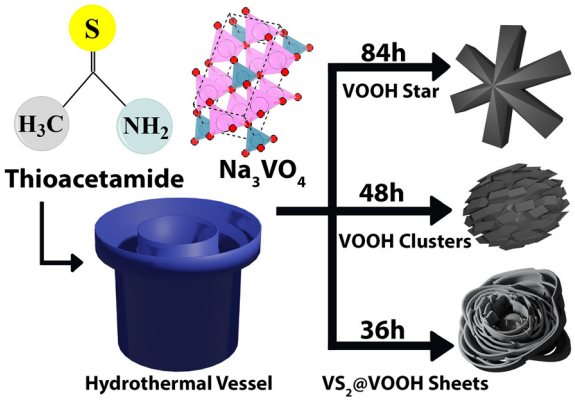

Fig. 2 Schematic representation of the synthetic procedure of vanadyl hydroxide stars.

ide, NaOH (50% w/w, CAS: 1310-73-2) and ultrapure water (18.1 MΩ using an Avidity Science Alto I water purification system) was used in the preparation of all the aqueous solutions.

Synthesis of VOOH structures. For all reactions, sodium orthovanadate was dried (highly hygroscopic) in a vacuum oven overnight; after drying, 1.122 mmol (0.2076 g) of sodium orthovanadate and 5.605 mmol (0.4231 g) of thioacetamide were dissolved in 15.00 ± 0.05 mL of ultrapure water and stirred for one hour at room temperature (schematic shown in Fig. 2). The resulting solution was then transferred into a 23 mL Teflon lined stainless steel autoclave and placed in a hot air oven at 160 °C for 36 h, 60 h, and 84 h. The hydrothermal vessels were allowed to cool down to room temperature inside the oven, and the black coloured precipitates were collected using a vacuum filtration system and washed with ultrapure water. The collected powder were then dried at 60 °C for 6 h.[38]

Synthesis of VS_2 sheets. Crystalline VS_2 synthesis was carried out by reaction of 1.122 mmol (0.2076 g) of sodium orthovanadate and 15.60 mmol (0.6167 g) of thioacetamide were dissolved in 15 ± 0.05 mL of ultrapure water and stirred for one hour at room temperature. The resulting solution was then transferred into a 23 mL Teflon lined stainless steel autoclave and placed in a hot air oven at 160 °C for 36 h. The hydrothermal vessels were allowed to cool down to room temperature, and the black-coloured precipitates were collected and washed using ultrapure water using a vacuum filtration system. The collected powder was dried at 60 °C for 6 h.

Synthesis of VS_4. VS_4 was synthesised using 1.122 mmol (0.1374 g) of sodium metavanadate as vanadium source and 5.605 mmol (0.4231 g) of thioacetamide were dissolved in 15.00 ± 0.05 mL of ultrapure water and stirred for one hour at room temperature. The pH of the reaction mixture was then adjusted to ~10 by the addition of NaOH solution. The resulting solution was then transferred into a 23 mL Teflon lined stainless steel autoclave and placed in a hot air at 160 °C with changes in reaction time.

2.2. Sample characterization

X-ray diffraction. Analysis of the crystal structure of the as-prepared powder samples was performed by X-ray diffraction. Diffracted intensities were measured on Rigaku XtaLABSynergy-S equipped with a HyPix-6000HE hybrid photon counting area detector. Powder diffraction experiments were performed using a Cu-target Photon Jet-S source with divergence slits set to provide a beam with 1.2 mrad. A Gandolfi data collection strategy (simultaneously scanning φ and ω) at a single κ orientation was used. Four detector positions were used to collect data to 80° in 2Θ at a detector distance of 60 mm. Samples were mounted using a 200 μm MiTeGen loop with Paratone-N oil. A background scan of the loop with oil was acquired to correct for background scatter.

Electron microscopy. The change in morphology of the resulting samples and the elemental analysis of the synthesized samples were carried out by field-emission scanning electron microscope (FESEM) with Oxford energy-dispersive X-ray spectrometer (EDS) – Hitachi SU70 detector. High-resolution transmission electron microscopy (HRTEM, Hitachi HT7800 operated at an accelerating voltage of 120 keV and JEOL JEM 2010), copper grids coated with an amorphous carbon film were used for the TEM measurements.

X-ray and Raman spectroscopy. Structural information on the composites were obtained by a Raman spectrometer (LabRAM HR by Horiba Scientific) with a laser wavelength of 532 nm excitation line from solid state lasers and a 600 grooves per mm grating. A 100× objective was used to focus the incident light and collect the Raman back scattered contribution. Typical measurements were conducted using a 200 μm slit. XANES experiments at the V K-edge were collected using an easyXAFS300+. The instrument is based on Rowland circle geometries with spherically bent crystal analysers (SBCAs) and a silicon drift detector (AXAS-M2, KETEK GmbH, Munich, Germany). For this, a Si (311) channel-cut monochromator was used to access the range 5450–5530 eV. All XANES spectra at the V K-edge were collected at room temperature in transmission mode for powder samples pellets which are mounted between two layers of Kapton tape. The collected data was then energy calibrated using a vanadium metal foil. Pre- and post-edge normalization was carried out as implemented by the Athena suite.

Inductive coupled plasma-mass spectroscopy (ICP-MS). Approximately 5 mg of powdered sample was digested in 5 mL concentrated HNO_3, followed by dilution with 42 mL deionized water to ensure complete dissolution and minimize matrix effects. The solution was filtered through a 0.22 μm PTFE membrane to remove particulates. From the filtrate, 37.7 μL aliquots were withdrawn and further diluted to 10 mL with 5% HNO_3 prior to measurement. This multistep dilution ensured analyte concentrations were within the linear calibration range of the instrument. Elemental quantification of vanadium was performed at the University at Buffalo Chemistry Instrument Centre (UBCIC), at the University at Buffalo, SUNY using a Thermo Scientific XSERIES 2 ICP-MS. The sample introduction system comprised a Burgener Ari Mist Nebulizer, a

peltier-cooled (4 °C) double-pass glass spray chamber, a quartz torch, and nickel sampler and skimmer cones. Sample transport from the ESI SC2 DX autosampler to the nebulizer was achieved *via* a peristaltic pump. The instrument was operated in kinetic energy dissociation (KED) mode to minimize interference using a gas mixture of 7% hydrogen in helium for the cell gas. Data acquisition and processing were performed using Thermo PlasmaLab software, with scandium and indium as internal standards. Elemental values are reported as mass fraction (%m/m) and ppb. Vanadium was quantified at ^{50}V (m/z 50) because the ^{51}V (m/z 51) channel exhibited matrix-dependent polyatomic interferences under our conditions (assigned to $^{34}S^{16}OH^+$), which can bias ^{51}V high. The ^{50}V channel yielded consistent replicate values following internal-standard correction and on-peak blank subtraction (Table S6).[39] Nevertheless, both ^{50}V and ^{51}V are reported for clarity.

Elemental analysis (EA). Sulfur was analyzed using a CE-Elantech, Inc. FlashSmart EA Analyzer 1112 series with C, H, N and S capability.

Methods for electrochemical testing

Electrode preparation. The working electrodes were prepared using synthesized vanadyl-based materials (VS_2@VOOH sheets, VS_2/VOOH clusters, and VOOH stars) as the active material. A composite slurry was prepared by mixing the active material, Super P conductive carbon black, and poly (vinylidene fluoride) (PVDF) in a weight ratio of 70 : 20 : 10. The mixture was dispersed in 1-methyl-2-pyrrolidinone (NMP, >99%) and stirred overnight to form a homogeneous slurry. This slurry was then cast onto 16 μm thick aluminium foil using a doctor blade to achieve a coating thickness of 50 μm. The coated foils were dried in a vacuum oven at 60 °C for 12 hours. Circular electrodes (15 mm in diameter) were punched out from the dried film, with an average active mass loading of 0.4 mg mm^{-2}.

Coin cell assembly. CR2032-type coin cells were assembled in an argon-filled Vigor glovebox (<1 ppm H_2O/O_2). Sodium metal (purchased from ThermoFisher Scientific) was used as both the counter and reference electrode. Whatman Grade 42 filter paper discs (19 mm diameter) served as the separators. The electrolyte consisted of 1.0 M sodium hexafluorophosphate ($NaPF_6$) dissolved in a 1 : 1 volume mixture of ethylene carbonate (EC, 99%) and dimethyl carbonate (DMC, 99%).

The Super P conductive carbon black was procured from MTI Corp. The binder, poly (vinylidene fluoride), was purchased from Alfa Aesar. The solvent, 1-methyl-2-pyrrolidinone (>99%), was purchased from ThermoFischer Scientific. For the current collectors, single sheet aluminium foil (thickness: 16 μm) was acquired from MTI Corp.

Electrochemical measurements. Galvanostatic charge–discharge cycling was performed using a BTS4000 Battery Testing Station (Neware) within the potential range of 0.1–4.0 V (*vs.* Na/Na^+). Cyclic voltammetry (CV) was conducted using a Squidstat Plus potentiostat (Admiral Instruments) at scan rates specified in the results section.

3. Results and discussion

Montroseite VOOH was obtained *via* a hydrothermal synthesis method for the reaction of sodium orthovanadate with thioacetamide as the reducing agent,[40–42] in which the solution was kept into a Teflon lined stainless steel autoclave and placed in a hot air oven at 160 °C for 36 h, 60 h, and 84 h. Li and collaborators discussed that the synthesis of VS_2 is highly dependent on the concentration of HS^- produced by the thermal decomposition of thioacetamide.[43] Indeed, we observe that at a concentration of thioacetamide corresponding to an approximately 15-fold mole excess relative to orthovanadate yielded VS_2 sheets with diameters of approximately 8–9 μm (Fig. 3a) at 36 h of reaction time. In contrast, when the thioacetamide was reduced to 5-fold excess mole ratio relative to orthovanadate, the product comprised VS_2@VOOH sheets (Fig. 3b) at 36 h of reaction time, consistent with the morphology previously reported by Li *et al.* in the literature.[40] This underpins the role of thioacetamide concentration in the formation of VS_2 and the further nucleation of VOOH.[40,43] Notwithstanding, clustered rods approximately 500 nm in length were observed at reaction time of 60 h (Fig. 3c) with a reduced presence of VS_2 in the XRD suggesting the oxygenation of VS_2 to VOOH. Nevertheless, initial formation of VOOH and VS_2 as separate nuclei cannot be ruled out since we observe the presence of VOOH in the XRD of a 24 h reaction (Fig. S2). With that said, the growth of VOOH on the surface of VS_2 has been previously reported under hydrothermal conditions where the initial formation VS_2 leads to an increased formation of $(NH_4)_2S$ adsorbed on the surface of VS_2 which promotes the formation of VS_3^- and eventual hydrolyzation to VOOH.[40] Furthermore, an additional consideration can be that VS_2 is redissolved into solution allowing V ions to form VOOH.[44] Both mechanisms require the eventual consumption of VS_2 to VOOH. Consistent with this, a set of proposed reactions pathway is described in eqn (S1)–(S10) in the SI where VS_2 is progressively consumed during the formation of VOOH. This spherical clustered morphology for VOOH has been previously reported for different reactions schemes that include $VO(acac)_2$ and cysteine or VO_3NH_4 with a reducing agent where a Kirkendall effect defines the canonical hollowed morphology.[45–47] The core void resulting from the Kirkendall effect are due to a nonreciprocal mutual diffusion process through the solid interface of two materials. In this case, as the initial nucleation of VOOH on the surface of VS_2 continues to grow, vanadium can be supplied from the VS_2 core, creating a hollow structure with VOOH rods growing from the edges of the sphere. Eqn (S11) in the SI summarizes the overall reaction pathway, showing that thioacetamide undergoes alkaline hydrolysis and react with vanadate ions to initially produce vanadium sulphide and the eventual formation of vanadium oxyhydroxide. Consistent with eqn (S1)–(S10), the reaction also produces sulphide by-products ($H_2S/HS^-/S^{2-}$ in eqn (S2), (S4), (S6) and (S7)) that can lead to elemental S_8 (eqn (S9) and (S10)) as observed in the XRD of this work (*vide infra*).[48,49] Ultimately, VOOH stars with diameters of 1.5–2 μm are observed at 84 h of reaction time

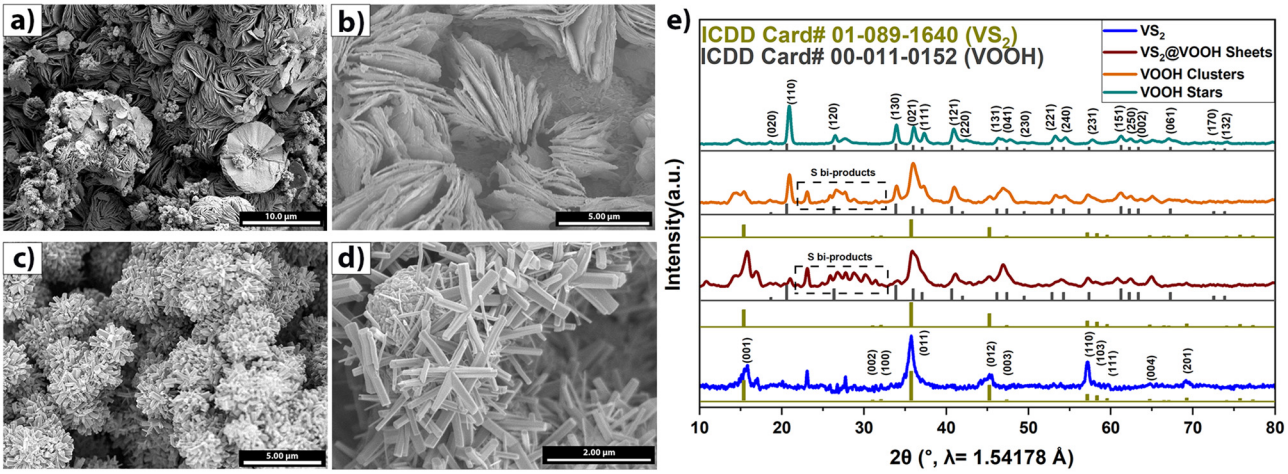

Fig. 3 High-resolution SEM images of (a) VS_2, (b) VS_2@VOOH sheets, (c) VOOH clusters, (d) VOOH stars and (e) X-ray diffraction patterns depicting the evolution of the morphology of VOOH stars.

(Fig. 3d). This is hitherto the first report of star-like morphology for VOOH.

3.1. Structural analysis

XRD pattern (Fig. 3e) for crystalline VS_2 sheets and VS_2@VOOH (reacted for 36 h) matches to a hexagonal crystal structure with space group $P\bar{3}m1$ consistent with JCPDS 01-089-1640.[50] The presence of reflections assigned to VOOH in the VS_2@VOOH samples confirms the growth of VOOH on the surface of the sheets. For clustered VOOH (reacted for 60 h) samples, we elucidate a significant decrease of the reflections associated with VS_2 and an increased presence of the orthorhombic phase for VOOH. Finally, the VOOH stars (reacted for 84 h) samples depict orthorhombic VOOH phase with no other phases observed. The full diffraction pattern for this sample can be indexed to the space group *Pbnm* of Montroseite VOOH (JCPDS 00-011-0152). Features observed near 15 2θ can be associated to noise resulting from background subtraction related to the sample holder in the XRD instrument (Fig. S3). The intense (110) reflection around 20.61 2θ suggests the preferential growth direction of the arms in the VOOH stars sample. The VS_2@VOOH and VOOH cluster samples show some sulphur impurities between 21.63 to 32.75 2θ which are not present in VOOH stars samples. In XRD, sulphur impurities can be indexed to α-S_8 (Fig. S4) with higher prevalence in sheets than rods.[40] Energy-dispersive X-ray spectrometry (EDS) measurements (Fig. S5) confirms the presence of vanadium, oxygen, and sulphur for sheets and rods. Interestingly, EDS measurement of the VOOH clusters show more relative concentration of sulphur than VS_2@VOOH sheets. The discrepancy between techniques could be due under sampling during the EDS measurement such that it is not capturing the true composition of the bulk sample. To address this discrepancy, inductively coupled plasma mass spectrometry (ICP-MS) and elemental analysis (EA) was performed for all three samples (shown in Table S6). Decrease of sulphur content upon progression to VOOH supports the hypothesis of VOOH nucleating at the expense of VS_2.[40] Finally, EDS of the VOOH stars clearly depicts the complete disappearance of S peaks, suggesting that the sulphur impurities could have oxidized into sulphates and washed off during filtration of the sample.

Raman spectroscopy, being a surface-sensitive technique, provides direct insight into the progressive transformation of VS_2 into VOOH. The pristine VS_2 sample exhibits characteristic modes at 104, 147.4, 199.3, 286.6, 305.1, 406.9, 483.0, 529.5, 703.2, and 996.6 cm^{-1}. Specifically, the modes around 286.6 cm^{-1} and 406.9 cm^{-1} correspond to the E_{1g} (in-plane) displacements of vanadium and A_{1g} (out-of-plane) vibration modes of the VS_2 structure, respectively, while the band at 703.2 cm^{-1} attributed to the rocking and stretching vibrations of V–S bonds, or their combination, indicating the preservation of key VS_2 structural motifs.[51–53] From the reaction scheme, the synthesis takes place under strongly basic, sulphide-rich conditions in which there is a probability of thiosulfate–sulphide exchange ($S_2O_3^{2-} + S^{2-} \rightleftharpoons S_3^{2-} + SO_3^{2-}$).[54] Such equilibrium can generate short-lived polysulfide species (S_x^{2-}), which are known to exhibit S–S stretching in the 430–520 cm^{-1} region. We therefore attribute the bands at 483 and 529.5 cm^{-1}, observed prominently in the pristine VS_2 sample, to polysulfide species or sulphur-rich by-products.[54] Consistent with this assignment, these bands disappear as the system transforms to VOOH, indicating that they are not intrinsic to the hydroxide phase. To the best of our knowledge, no prior Raman studies of VS_2 have reported these specific modes, supporting our interpretation that they originate from reaction-dependent sulphur species rather than the bulk VS_2 lattice. Upon nucleation of VOOH over the VS_2 sheets, the peaks originating from VS_2 exhibit a red shift, suggesting the initial formation of the VOOH on the surface of the layers. With progression to VOOH rods, all Raman modes are retained from VS_2@VOOH, confirming that these features correspond predominantly to the hydroxide phase. For the VOOH stars,

most modes undergo further red-shifts relative to the rods, consistent with increased lattice strain, where the bands at 192.8 and 280.7 cm^{-1} are assigned to the B_{2g} bending vibrations of the O_C–V–O_B linkages, where O_C and O_B denote corner-sharing and bridging oxygen atoms within the VO_6 polyhedral framework, respectively.[55] The 405.3 cm^{-1} is assigned to V–O–V bending in edge-sharing octahedra and 685.5 cm^{-1} to V–O–V stretching/rocking.[55] In contrast, the high-frequency vibration exhibits a blue-shift from 992.7 to 998.6 cm^{-1} assigned to the axial V–O stretching. This blue-shift is attributed to strengthening of the short V–O bond as a result of dehydration during the olation–oxolation that drives star formation.[56] These non-uniform shifts in vibrational modes highlight localized strain and altered bonding environments rather than a uniform structural distortion. The overall similarity stems from local structure where their lowest-energy phonons are dominated by metal-center and V–X (X = S, O/OH) bending modes that fall in the same spectral range. During the VS_2 to VOOH conversion, short-range octahedral connectivity is largely retained, therefore we observe small shifts in the phonon excitation range.[52,57] Together, these spectral features reveal critical insights into the structural evolution during the transition from sulphide to hydroxide phases and highlight how strain effects and coordination changes influence the vibrational landscape.

We decided to elucidate the changes in electronic structure across morphologies to explore fundamental redox processes that occur during the nucleation and growth (Fig. 4b). First, we focused on the V K-edge where the pre-edge (approx. 5470 eV) is assigned to dipole forbidden transitions from 1s core states to 3d states that become increasingly allowed with hybridization with p-orbitals from the coordinating ligand (O 2p and/or S 3p). In comparison, the main edge (approx. 5489 eV) represents dipole allowed transitions from V 1s to V 4p states.[58–61] A stark shift to lower eV and initial decrease in the intensity of the pre-edge is observed for VS_2 crystallites and VS_2@VOOH. This change in intensity can be associated to the extent of VOOH grown on the surface of VS_2 and rationalized as the result of the increased presence of V^{3+} from VOOH, the changes in chemical nature of the ligands, and the vanadium coordination environment prove to be consequential to this change.[58,60,62,63] From VS_2@VOOH to VOOH clusters the intensity of the pre-edge slightly decreases and stays consistent in VOOH stars, further confirming the transformation to VOOH at 60 h, as observed from the diffraction pattern and Raman spectroscopy. To fundamentally understand the nature of the electronic structure of the produced samples, we compared the resulting VOOH to bulk vanadium oxide standards (Fig. S7a). Interestingly, the offset (E_0) for the VOOH samples raises between V_2O_3 (V^{3+}) and VO_2 (V^{4+}), suggesting the coexistence of $V^{3+/4+}$. This observation is consistent with previous reports on vanadium oxyhydroxides, where mixed-valence states were inferred based on the correlation between the oxidation state and the rising edge position, corresponding to 50% of the normalized absorbance. The E_0 value shifts linearly to higher energies with increasing mean oxidation state. Such trends were clearly observed in the study by Besnardiere *et al.*, where the E_0 values for vanadium oxyhydroxide phases (*e.g.*, Duttonite and Häggite) provided unambiguous evidence of the oxidation states for the vanadium.[64] To further support this mixed-valence assignment, we plotted the absorption edge offsets (E_0 = 0.5) of our samples alongside vanadium standards and synthesized samples(Fig. S7b). This graphical representation, places E_0 values on the *x*-axis and sample identity on the *y*-axis, clearly demonstrates that the VOOH sample falls between V_2O_3 (V^{3+}) and VO_2 (V^{4+}), reinforcing the presence of a mixed $V^{3+/4+}$ oxidation state. The coexistence of V^{3+} and V^{4+} observed in our VOOH samples can be attributed to the charge

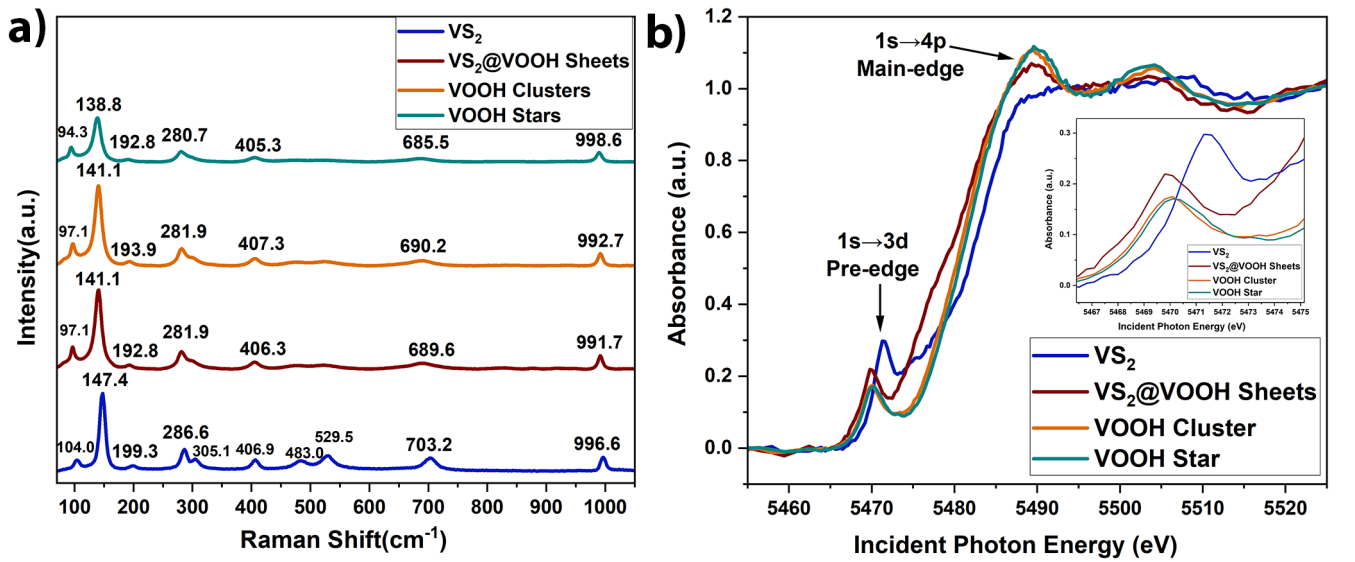

Fig. 4 (a) Raman spectra and (b) X-ray absorption spectra (XAS) for the vanadium K-edge for the resulting samples across different reaction times.

compensation related to nonstoichiometric vanadium oxyhydroxide resulting from possible imbalances in the olation–oxolation process. Similar mixed-valent stabilization *via* oxygen self-doping has been reported previously in hollandite vanadium oxyhydroxides.[65]

High-resolution transmission electron microscopy images were taken for nanostars (Fig. 5a–c) and the selected-area electron diffraction (SAED) pattern (d) for VOOH. The existence of grain boundaries at the intersection of the small rods suggests that the nucleation and growth of the nanostar go through coalescing small VOOH rods that produce twinned boundaries. This is further confirmed by SAED pattern (Fig. 3d) with the electron beam directed along [001] axis.[66] Following this pattern, we can develop a proposed atomic arrangement that further confirms the evolution into a hexagonally shaped star. We hypothesize the following nucleation and growth process: first, the surface of VS_2 is hydroxylated producing the first seeds of VOOH. Then, VOOH grows on the surface through an olation condensation where hydroxyl bridge is formed between two metal bridges.[36,37,67] As time progresses, some of the VOOH rods separate from the clusters which then allow for the growth of nanostars through an oxolation process (Fig. S1) resulting in the observed boundaries and resulting morphology for VOOH. We were curious of why this growth hasn't been seen in the literature and noticed that most use sodium metavanadate as the vanadium source for VOOH.

Following the same procedure, we initially observed that the reaction solution with sodium orthovanadate (pH 10) produced VOOH stars, whereas sodium metavanadate (pH 7.4) produced only VS_4 sheets (Fig. S8 and S9), suggesting that pH could be a major consideration in the growth of star morphology. To test this, we performed control reactions with sodium metavanadate after adjusting the solution pH to 10 with NaOH. However, these reactions resulted in VS_4 sheet-like morphologies at all reaction times (Fig. S10 and S11), demonstrating that pH alone is not sufficient to account for the formation of nanostars. Instead, the outcome is governed primarily by the structural nature of the precursors: orthovanadate consists of discrete VO_4^{3-} tetrahedra that are more reactive under hydrothermal conditions, which allowed reaction conditions discussed in eqn (1)–(10) and led to star architectures. In contrast, metavanadate exists as extended VO_3^- polymeric chain structures favouring assembly of two-dimensional sheets. Thus, while alkaline conditions accelerate nucleation kinetics, the inherent precursor speciation is the decisive factor controlling morphology.

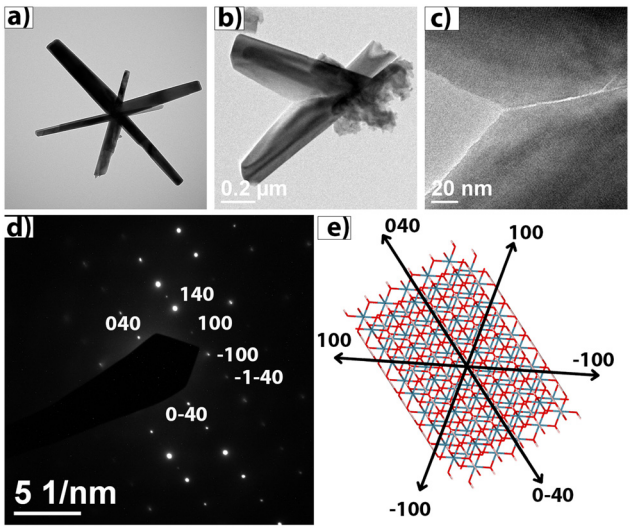

Fig. 5 (a) TEM images of VOOH stars, (b and c) assembled rods, (d) SAED Pattern and (e) atomic arrangement projected along [001] of Montroseite VOOH.

3.2. Electrochemical performance

The galvanostatic cycling was evaluated over 300 cycles with a current density of 0.05 A g^{-1}. Fig. 6a shows that VOOH stars had higher initial capacity (160 mAh g^{-1}) compared to VS_2@VOOH (130.07 mAh g^{-1}) and VOOH clusters (125 mAh g^{-1}) and the discharged capacity of VS_2@VOOH sheet decays drastically in the initial cycles before it stabilizes over 300 cycles at 54 mAh g^{-1}. This same behaviour can be seen for the clustered rods initial drop in capacity before stabilizing after 50 cycles. VOOH nanostars shown the remarkable cycling performance for 300 cycles and deliver higher capacity in comparison to the sheets and clusters through 300 cycles. The high initial specific capacities observed during galvanostatic charge–discharge measurements suggest a relatively unobstructed diffusion of Na ions into the electrode material, indicating good ionic accessibility and efficient electrochemical kinetics at the initial stages of cycling. Cyclic voltammogram (CV) of the active material electrode in the potential range of 4–0.1 V *vs.* Na/Na^+ at a scanning rate of 0.1 mV s^{-1} is shown in Fig. 5(b and c). For the VS_2@VOOH sheets, two sharp and well-defined redox peaks appear at approximately 1.55 V and 2.45 V, corresponding to reversible sodium-ion intercalation/deintercalation processes. These redox features diminish markedly after the second cycle, consistent with the galvanostatic cycling results that show rapid capacity decay and highlight the poor reversibility of the faradaic reactions. The pronounced current response in the first cycle is typically associated with initial Na^+ insertion and the formation of a solid electrolyte interphase (SEI). The diminished intensity in subsequent cycles can be attributed to the reduced availability of free active sites and the build-up of diffusion resistance, in contrast to the more ideal, reversible behaviour often reported for pristine VS_2.[40] In addition, a small number of distinct redox events are observed for VOOH clusters and nanostars, which appear during the extended cycles. The reduction events 0.4 V, 1.0 V and oxidation peak at 1.8 V can be regarded as the reversible intercalation/deintercalation of Na ions in VOOH cluster and VOOH star. Interestingly, the VOOH clusters display redox peaks at 1.5 and 2.3 V, which we attribute to the concurrent presence of VS_2 and VOOH in the first cycle. However, the VS_2-associated signals diminish rapidly after the initial cycle, while the VOOH-related reduction peaks at 0.4 and 1.0 V and the oxi-

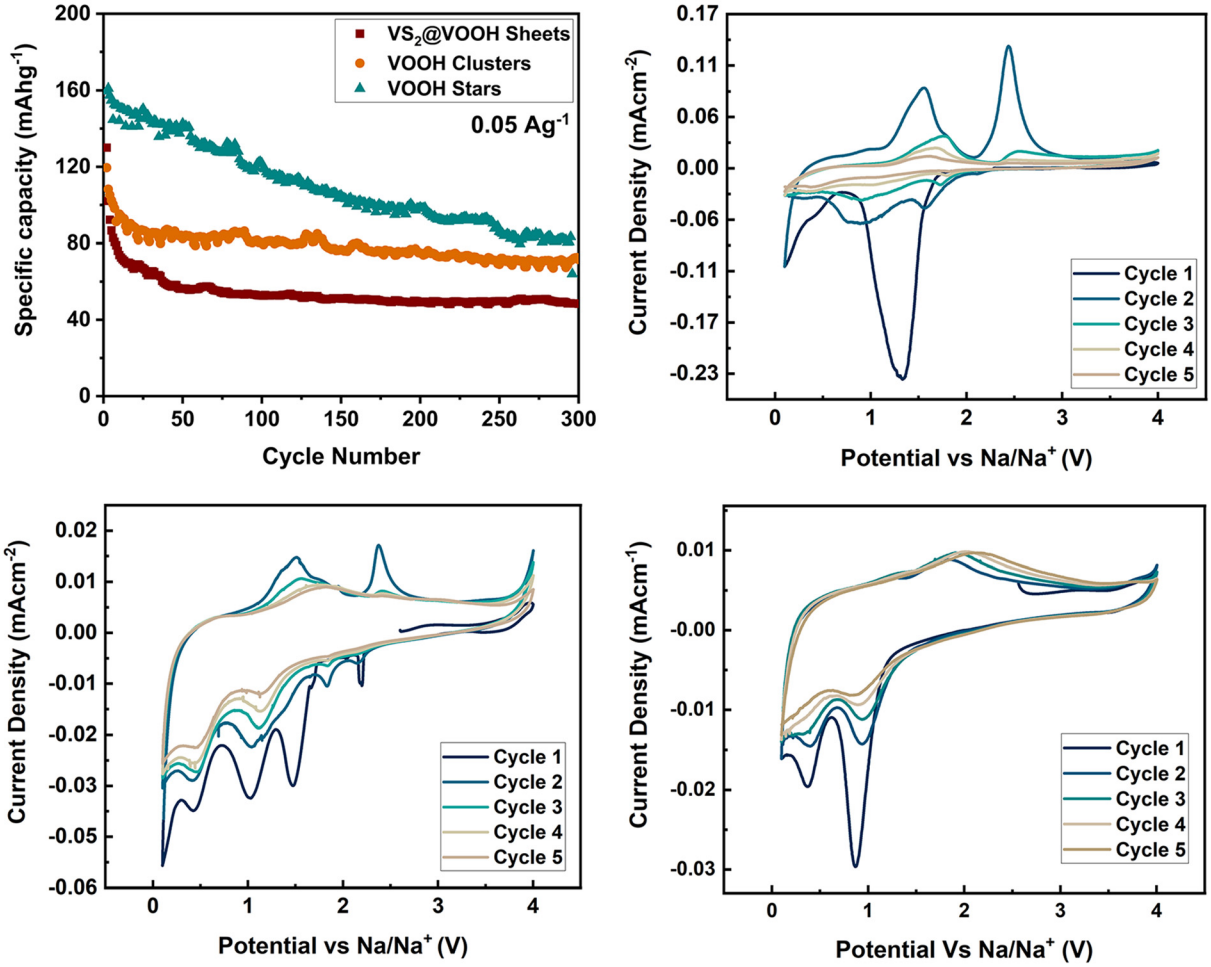

Fig. 6 (a) Stability of the samples over 300 cycles and cyclic voltammetry experiments for (b) VS_2@VOOH sheets, (c) VOOH cluster, and (d) VOOH stars.

dation peak at 1.8 V remain intense and consistent, indicating that VOOH dominates the redox activity in subsequent cycles.

$$VS_2 + x\mathrm{Na}^+ + xe^- \rightarrow \mathrm{Na}_x\mathrm{VS}_2$$

$$\mathrm{VOOH} + x\mathrm{Na}^+ + xe^- \rightarrow \mathrm{Na}_x\mathrm{VOOH}$$

For VOOH cluster and VOOH nanostar later cycles shows a symmetric rectangular shape, typical of pseudocapacitive behaviour, which is the proposed electrochemical mechanism for VOOH samples.[68]

4. Conclusions

In summary, we have reported the synthetic conditions to produce VOOH with a star morphology highly dependent on reaction time and vanadium source. We proposed that VS_2 sheets are coated by VOOH seeds which grow into VOOH clustered rods through olation mechanism. These rods separate and through oxolation of the particles grow into six-fold star structure. This work highlights the need to understand fundamental nucleation and growth mechanisms that result in materials with strained morphologies. Also, the electrochemical evaluations indicate the pseudocapacitive behaviour of VOOH stars delivering excellent cyclic stability for first 300 cycles in comparison to VS_2@VOOH sheets and VOOH clusters. While other contributors like composition, oxidation state, and defect chemistry may also play a role in electrochemical behaviour of this system, this work highlights the need to further explore the correlation between morphology and changes in nonstoichiometric compositions, disproportion of oxidation states, and increased density of defects which has a direct relationship to tailoring electrochemical behaviour, work that is currently underway in our research laboratory.

Author contributions

The manuscript was written with the contribution of all authors. L. D. J. B. designed the research and work plan. J. S., T. J. K., K. M. P. C., and C. V. did the synthesis, characteriz-

ations, data plots, and analysing data for the vanadium samples. M. J. and C. Y. L. carried out and analysed the electrochemical experiments. J. S. and L. D. J. B. drafted the manuscript and all authors revised it. All authors approved the submitted manuscript.

Conflicts of interest

There are no conflicts to declare.

Data availability

The authors confirm that the data supporting the findings of this study are available within the article and more data can be available from the corresponding author on request.

Supplementary information (SI) is available. See DOI: https://doi.org/10.1039/d5nr02771c.

Acknowledgements

We would Like to acknowledge Rigaku Xta LAB Synergy-S, a part of the Chemistry Instrument Centre (CIC) at University at Buffalo (UB), was purchased with NSF CHE-2216151. We also acknowledge the Thermo Scientific XSERIES 2 ICP-MS at the University at Buffalo Chemistry Instrument Centre (UBCIC), which was supported by NSF CHE-0959565. Financial support from the Alfred P. Sloan Foundation (Grant No. G-2021-17076) is also acknowledged, which facilitated the summer research experience of K. M. P. C. to contribute to this project.

References

1 W. Xu, S. Li, S. Zhou, J. K. Lee, S. Wang, S. G. Sarwat, X. Wang, H. Bhaskaran, M. Pasta and J. H. Warner, *ACS Appl. Mater. Interfaces*, 2018, **10**, 4630–4639.
2 S. Wang, J. Li, S. Hu, H. Kang, S. Zhao, R. Xiao, Y. Sui, Z. Chen, S. Peng, Z. Jin, X. Liu, Y. Zhang and G. Yu, *ACS Appl. Nano Mater.*, 2022, **5**, 2273–2279.
3 M. Ardahe, M. R. Hantehzadeh and M. Ghoranneviss, *J. Electron. Mater.*, 2020, **49**, 1002–1008.
4 D. Senapati, A. K. Singh and P. C. Ray, *Chem. Phys. Lett.*, 2010, **487**, 88–91.
5 R. C. Miller, R. H. Geiss and A. L. Prieto, *ACS Nano*, 2021, **15**, 11981–11991.
6 R. G. Weiner, M. R. Kunz and S. E. Skrabalak, *Acc. Chem. Res.*, 2015, **48**, 2688–2695.
7 Y. Xia, X. Xia and H.-C. Peng, *J. Am. Chem. Soc.*, 2015, **137**, 7947–7966.
8 Y. Yin, C. Erdonmez, S. Aloni and A. P. Alivisatos, *J. Am. Chem. Soc.*, 2006, **128**, 12671–12673.
9 J. Polte, *CrystEngComm*, 2015, **17**, 6809–6830.
10 S. E. Habas, H. Lee, V. Radmilovic, G. A. Somorjai and P. Yang, *Nat. Mater.*, 2007, **6**, 692–697.
11 F.-R. Fan, D.-Y. Liu, Y.-F. Wu, S. Duan, Z.-X. Xie, Z.-Y. Jiang and Z.-Q. Tian, *J. Am. Chem. Soc.*, 2008, **130**, 6949–6951.
12 J. D. Smith, M. M. Scanlan, A. N. Chen, H. M. Ashberry and S. E. Skrabalak, *ACS Nano*, 2020, **14**, 15953–15961.
13 J. D. Smith, Z. J. Woessner and S. E. Skrabalak, *J. Phys. Chem. C*, 2019, **123**, 18113–18123.
14 L. Whittaker, J. M. Velazquez and S. Banerjee, *CrystEngComm*, 2011, **13**, 5328–5336.
15 A. P. Rooney, Z. Li, W. Zhao, A. Gholinia, A. Kozikov, G. Auton, F. Ding, R. V. Gorbachev, R. J. Young and S. J. Haigh, *Nat. Commun.*, 2018, **9**, 3597.
16 R. Wang, X. Chen, Z. Huang, J. Yang, F. Liu, M. Chu, T. Liu, C. Wang, W. Zhu, S. Li, S. Li, J. Zheng, J. Chen, L. He, L. Jin, F. Pan and Y. Xiao, *Nat. Commun.*, 2021, **12**, 3085.
17 J. Wang, X. Zhao, G. Zou, L. Zhang, S. Han, Y. Li, D. Liu, C. Fernandez, L. Li, L. Ren and Q. Peng, *Mater. Today Nano*, 2023, **22**, 100336.
18 W. Yu, S. Li and C. Huang, *RSC Adv.*, 2016, **6**, 7113–7120.
19 A. L. Siegel and G. A. Baker, *Nanoscale Adv.*, 2021, **3**, 3980–4004.
20 J. L. Andrews, A. Mukherjee, H. D. Yoo, A. Parija, P. M. Marley, S. Fakra, D. Prendergast, J. Cabana, R. F. Klie and S. Banerjee, *Chem*, 2018, **4**, 564–585.
21 J. V. Handy, J. L. Andrews, B. Zhang, D. Kim, N. Bhuvanesh, Q. Tu, X. Qian and S. Banerjee, *Cell Rep. Phys. Sci.*, 2022, **3**, 100712.
22 L. R. De Jesus, Y. Zhao, G. A. Horrocks, J. L. Andrews, P. Stein, B.-X. Xu and S. Banerjee, *J. Mater. Chem. A*, 2017, **5**, 20141–20152.
23 L. R. De Jesus, G. A. Horrocks, Y. Liang, A. Parija, C. Jaye, L. Wangoh, J. Wang, D. A. Fischer, L. F. J. Piper, D. Prendergast and S. Banerjee, *Nat. Commun.*, 2016, **7**, 12022.
24 C. Guo, S. Yi, R. Si, B. Xi, X. An, J. Liu, J. Li and S. Xiong, *Adv. Energy Mater.*, 2022, **12**, 2202039.
25 A. Parija, Y. Liang, J. L. Andrews, L. R. De Jesus, D. Prendergast and S. Banerjee, *Chem. Mater.*, 2016, **28**, 5611–5620.
26 P. M. Marley, G. A. Horrocks, K. E. Pelcher and S. Banerjee, *Chem. Commun.*, 2015, **51**, 5181–5198.
27 H. Shi, H. Liang, F. Ming and Z. Wang, *Angew. Chem., Int. Ed.*, 2017, **56**, 573–577.
28 J. Zhang, R. Cui, C. Gao, L. Bian, Y. Pu, X. Zhu, X. Li and W. Huang, *Small*, 2019, **15**, e1904688.
29 X. Zhang, Y. Liu, C. Li, L. Tian, F. Yuan, S. Zheng and Z. Sun, *Chem. Eng. J.*, 2022, **429**, 132374.
30 Y.-X. Zhang and Y. Jia, *Appl. Surf. Sci.*, 2014, **290**, 102–106.
31 L. Wang, K.-W. Huang, J. Chen and J. Zheng, *Sci. Adv.*, 2019, **5**, eaax4279.
32 F. Sari, S. Abdillah and J.-M. Ting, *Chem. Eng. J.*, 2021, **416**, 129165.
33 Y. Xu, L. Zheng and Y. Xie, *Dalton Trans.*, 2010, **39**, 10729–10738.
34 H. Fei, X. Ding, M. Wei and K. Wei, *Solid State Sci.*, 2011, **13**, 2049–2054.

35 Z. Ren, Y. Zhang, Y. Liu and C. Meng, *Mater. Lett.*, 2024, **377**, 137437.
36 J.-P. Jolivet, E. Tronc and C. Chanéac, *C. R. Geosci.*, 2006, **338**, 488–497.
37 J.-P. Jolivet, C. Chanéac and E. Tronc, *Chem. Commun.*, 2004, 481–483, DOI: 10.1039/B304532N.
38 C. S. Rout, B. H. Kim, X. Xu, J. Yang, H. Y. Jeong, D. Odkhuu, N. Park, J. Cho and H. S. Shin, *J. Am. Chem. Soc.*, 2013, **135**, 8720–8725.
39 V. Chrastný, M. Komárek, M. Mihaljevic and J. Stíchová, *Anal. Bioanal. Chem.*, 2006, **385**, 962–970.
40 W. Li, J. Huang, L. Feng, L. Cao, Y. Feng, H. Wang, J. Li and C. Yao, *J. Mater. Chem. A*, 2017, **5**, 20217–20227.
41 J. K. Das, A. K. Samantara, A. K. Nayak, D. Pradhan and J. N. Behera, *Dalton Trans.*, 2018, **47**, 13792–13799.
42 A. B, N. Kottam and C. S. K B, *Mater. Today: Proc.*, 2021, **46**, 545–549.
43 W. Li, J. Huang, L. Feng, L. Cao, Y. Feng, H. Wang, J. Li and C. Yao, *J. Mater. Chem. A*, 2017, **5**, 20217–20227.
44 Y. Zhang, Y. Chen, Y. Jiang, J. Wang, X. Zheng, B. Han, K. Xia, Q. Gao, Z. Cai, C. Zhou and R. Sun, *Adv. Funct. Mater.*, 2023, **33**, 2212785.
45 L. Wu, A. Teng, M. Li, L. Li, Z. Huang, X. Li, J. Yu, S. Xu, F. Zou, A. Zou, J. Zhang, T. Jiang, Y. Xin, X. Hu and G. Li, *Mater. Horiz.*, 2024, **11**, 1098–1107.
46 Y. Xu, L. Zheng and Y. Xie, *Dalton Trans.*, 2010, **39**, 10729–10738.
47 Z. Yang, N. Yang and M.-P. Pileni, *J. Phys. Chem. C*, 2015, **119**, 22249–22260.
48 R. Steudel, *Ind. Eng. Chem. Res.*, 1996, **35**, 1417–1423.
49 T. Siu and C. Q. Jia, *Ind. Eng. Chem. Res.*, 1999, **38**, 3812–3816.
50 S. A. Patil, I. Rabani, S. Hussain, Y. S. Seo, J. Jung, N. K. Shrestha, H. Im and H. Kim, *Nanomaterials*, 2022, **12**, 339.
51 W. Fang, H. Zhao, Y. Xie, J. Fang, J. Xu and Z. Chen, *ACS Appl. Mater. Interfaces*, 2015, **7**, 13044–13052.
52 P. He, M. Yan, G. Zhang, R. Sun, L. Chen, Q. An and L. Mai, *Adv. Energy Mater.*, 2017, **7**, 1601920.
53 D. S. Patil, I. Rabani, S. Hussain, Y.-S. Seo, J. Jung, N. K. Shrestha and H. Im, *Nanomaterials*, 2022, **12**, 339.
54 C. Nims, B. Cron, M. Wetherington, J. Macalady and J. Cosmidis, *Sci. Rep.*, 2019, **9**, 7971.
55 B. Ali, C. Aykaç and B. Güzeldir, *Appl. Phys. A*, 2019, **125**, 6308581.
56 F. D. Hardcastle and I. E. Wachs, *J. Phys. Chem.*, 1991, **95**, 5031–5041.
57 G. Backes, J. H. Enemark and T. M. Loehr, *Inorg. Chem.*, 1991, **30**, 1839–1842.
58 J. Wong, F. W. Lytle, R. P. Messmer and D. H. Maylotte, *Phys. Rev. B: Condens. Matter Mater. Phys.*, 1984, **30**, 5596–5610.
59 A. J. Hobson, D. I. Stewart, A. W. Bray, R. J. G. Mortimer, W. M. Mayes, A. L. Riley, M. Rogerson and I. T. Burke, *Sci. Total Environ.*, 2018, **643**, 1191–1199.
60 C. Tang, P. Georgopoulos, M. E. Fine, J. B. Cohen, M. Nygren, G. S. Knapp and A. Aldred, *Phys. Rev. B: Condens. Matter Mater. Phys.*, 1985, **31**, 1000–1011.
61 G. A. Sawatzky and D. Post, *Phys. Rev. B: Condens. Matter Mater. Phys.*, 1979, **20**, 1546–1555.
62 J. Wong, F. W. Lytle, R. P. Messmer and D. H. Maylotte, *Phys. Rev. B: Condens. Matter Mater. Phys.*, 1984, **30**, 5596–5610.
63 L. Zhang, D. Sun, Q. Wei, H. Ju, J. Feng, J. Zhu, L. Mai, E. J. Cairns and J. Guo, *J. Phys. D: Appl. Phys.*, 2018, **51**, 494001.
64 J. Besnardiere, X. Petrissans, F. Ribot, V. Briois, C. Surcin, M. Morcrette, V. Buissette, T. Le Mercier, S. Cassaignon and D. Portehault, *Inorg. Chem.*, 2016, **55**, 11502–11512.
65 I. Djerdj, D. Sheptyakov, F. Gozzo, D. Arčon, R. Nesper and M. Niederberger, *J. Am. Chem. Soc.*, 2008, **130**, 11364–11375.
66 H. G. Liao, Y.-X. Jiang, Z.-Y. Zhou, S.-P. Chen and S.-G. Sun, *Angew. Chem., Int. Ed.*, 2008, **47**, 9100–9103.
67 D. Portehault, S. Cassaignon, E. Baudrin and J.-P. Jolivet, *Cryst. Growth Des.*, 2010, **10**, 2168–2173.
68 J. Shao, Y. Ding, X. Li, Z. Wan, C. Wu, J. Yang, Q. Qu and H. Zheng, *J. Mater. Chem. A*, 2013, **1**, 12404–12408.